

PROPAGATING WAVES AND MAGNETOHYDRODYNAMIC MODE COUPLING IN THE QUIET-SUN NETWORK

D. SHAUN BLOOMFIELD,¹ R. T. JAMES MCAITEER,¹ MIHALIS MATHIOUDAKIS,¹ DAVID R. WILLIAMS,² AND FRANCIS P. KEENAN¹

Received 2003 August 14; accepted 2003 December 16

ABSTRACT

High-cadence multiwavelength optical observations were taken with the Dunn Solar Telescope at the National Solar Observatory, Sacramento Peak, accompanied by Advanced Stokes Polarimeter vector magnetograms. A total of 11 network bright points (NBPs) have been studied at different atmospheric heights using images taken in wave bands centered on $\text{Mg I } b_1 - 0.4 \text{ \AA}$, $\text{H}\alpha$, and Ca II K_3 . Wavelet analysis was used to study wave packets and identify traveling magnetohydrodynamic waves. Wave speeds were estimated through the temporal cross-correlation of signals, in selected frequency bands of wavelet power, in each wavelength. Four mode-coupling cases were identified, one in each of four of the NBPs, and the variation of the associated Fourier power with height was studied. Three of the detected mode-coupling, transverse-mode frequencies were observed in the 1.2–1.6 mHz range (mean NBP apparent flux density magnitudes over 99–111 Mx cm^{-2}), with the final case showing 2.0–2.2 mHz (with 142 Mx cm^{-2}). Following this, longitudinal-mode frequencies were detected in the range 2.6–3.2 mHz for three of our cases, with 3.9–4.1 mHz for the remaining case. After mode coupling, two cases displayed a decrease in longitudinal-mode Fourier power in the higher chromosphere.

Subject headings: MHD — Sun: chromosphere — Sun: magnetic fields — Sun: oscillations — Sun: photosphere

1. INTRODUCTION

Emission from the chromosphere is commonly separated into the “nonmagnetic” internetwork and the “magnetic” network. The internetwork is generally defined as the interior of supergranular cells, where magnetic bipolar elements emerge at the photosphere, quickly drift apart, and split into unipolar elements (Schrijver et al. 1997). These magnetic elements are subsequently transported to cell boundaries through supergranular flow, where they may coalesce, creating the stronger field network. Network bright points (NBPs) are observed in intergranular lanes at the supergranular cell boundary, becoming more concentrated at granular and supergranular vertices and typically corresponding to sites of kilogauss magnetic fields (Berger & Title 2001). Internetwork regions mainly exhibit atmospheric variations at frequencies greater than 4 mHz (commonly in grains; see the review paper by Rutten & Uitenbroek 1991), and the dynamics of these regions have been successfully modeled by Carlsson & Stein (1997), using acoustic shocks driven by the measured velocities of the photospheric $\text{Fe I } \lambda 3966.8$ line (Lites, Rutten, & Kalkofen 1993). These simulations achieved good agreement with the observed Ca II H profiles, specifically in the production of Ca II H_{2V} grains. By contrast, the network is known to show variations at frequencies ≤ 4 mHz (e.g., Damé, Gouttebroze, & Malherbe 1984; Lites et al. 1993; Cauzzi, Falchi, & Falciani 2000), suggesting a different heating mechanism.

Chromospheric heating theories require energy production and transport to the chromosphere, with subsequent deposition of this energy. The mechanisms involved often result from or lead to some manner of oscillatory behavior. For example,

Kneer & von Uexküll (1985, 1986) interpret low-frequency oscillations in the supergranular cell boundary as the result of stochastic footpoint motions of flux tubes. Further work by von Uexküll et al. (1989) claimed that the magnetic energy dissipated through random field reorganization, caused by these footpoint motions, can balance the radiative losses in the upper chromosphere. More recently, Goodman (2000) suggested that linear, slow, long-period, longitudinal magnetoacoustic waves drive charged-particle Pedersen currents, which in turn heat the plasma in thin flux tubes in the chromospheric network through resistive dissipation.

Analytical modeling has recently shown that transverse-mode magnetohydrodynamic (MHD) waves are capable of exciting atmospheric oscillations with 7–10 minute periods (~ 1.5 – 2.5 mHz), while longitudinal-mode waves excite those near 3 minutes (~ 5.5 mHz; Musielak & Ulmschneider 2003a, 2003b). This suggests that oscillations in the nonmagnetic internetwork are consistent with the longitudinal-mode processes modeled in magnetic flux tubes, while those oscillations observed in the magnetic network are more closely related to transverse-mode processes in magnetic flux tubes. Although capable of carrying energy into the chromosphere, transverse-mode MHD waves cannot dissipate, since they are noncompressive. However, longitudinal modes are compressive and can deposit their energy through shocking in the atmosphere (Zhugzhda, Bromm, & Ulmschneider 1995). Kalkofen (1997) proposed a heating mechanism based on the transformation of transverse wave modes at frequency ν_κ to longitudinal modes at frequency ν_λ ($\approx 2\nu_\kappa$). Using the Klein-Gordon equation, Hasan & Kalkofen (1999) modeled the generation of decoupled, linear, transverse- and longitudinal-mode waves in a thin flux tube through external granular buffeting. They found the energy flux of the transverse mode to be an order of magnitude greater than that of the longitudinal mode for typical NBP field strengths, indicating preferential transverse-mode generation from the photosphere.

¹ Department of Pure and Applied Physics, Queen’s University Belfast, Belfast BT7 1NN, Northern Ireland, UK; s.bloomfield@qub.ac.uk.

² Mullard Space Science Laboratory, Holmbury St. Mary, Dorking, Surrey RH5 6NT, UK.

Continuing their work, Hasan et al. (2003) investigated the propagation of coupled, nonlinear, transverse and longitudinal modes. They determined that the effective onset of longitudinal modes occurs when the transverse velocity amplitude is ~ 0.3 of the transverse-mode tube speed and, through nonlinear effects, becomes efficient when these two speeds are comparable. After mode transformation, the remaining transverse modes may continue propagating higher into the atmosphere while the longitudinal modes would be expected to shock, hence dissipating their energy.

In an earlier paper, McAteer et al. (2003) used an image segmentation technique to separate the network from the internetwork in order to study NBP oscillations at various heights within the solar chromosphere. They showed that candidates for MHD mode-coupling cases can be found through novel wavelet analysis techniques, extending the wealth of Fourier oscillation studies into the time-localized domain. In the present paper, we use high-cadence imaging to constrain wave speeds and provide magnetic field information for a large number of NBPs. Using multiwavelength optical observations, we search for wave signatures at different heights in the solar atmosphere. In § 2 we describe the observations, while the data reduction and analysis techniques are outlined in § 3. A summary of all detected waves is then presented in § 4, alongside an overview of the mode-coupling cases observed. Finally, from these discussions our conclusions are drawn in § 5.

2. OBSERVATIONS

The data presented here are part of an observing sequence obtained on 2002 July 11, with the Richard B. Dunn Solar Telescope (DST) at the National Solar Observatory, Sacramento Peak. A number of instruments were employed to image a $130'' \times 130''$ region of the quiet Sun, tracking solar rotation from an initial pointing of disk center (heliocentric coordinates $[0'', 0'']$). A Zeiss universal birefringent filter (UBF; Beckers, Dickson, & Joyce 1975) was used with a 1024×1024 pixel CCD detector to cycle through a number of wavelengths. The data consist of 377 images in each wavelength, taken with a 10 s cadence. In addition, a Halle birefringent filter was employed with a 512×512 CCD detector to obtain simultaneous images in Ca II K₃. The exposure time and subsequent readout time required for each Ca II K₃ image allowed a complete UBF cycle to be performed, resulting in identical cadence in each spectral band. Table 1 lists the wavelengths and filter passbands used in the image acquisition, alongside their approximate heights of formation. It should be noted that the formation heights of Vernazza, Avrett, & Loeser (1981) are obtained for the average quiet Sun and as such may not be suitable for magnetic regions. The resulting UBF and Ca II K₃ images have a pixel resolution of $0''.15$ and $0''.29$ pixel⁻¹, respectively. The selection of a portion of quiet

Sun, which was spatially removed from regions of heightened activity (i.e., active regions), coupled with moderate-to-poor periods of seeing, meant that the complete adaptive optics system was unable to be used (because of the lack of a distinct, stable structure such as a sunspot), instead allowing only tip-tilt corrections to be applied.

Cospatial and cotemporal photospheric magnetic field information was obtained with the Advanced Stokes Polarimeter (ASP; Elmore et al. 1992). Photospheric maps of the central portion of the same field of view (FOV) as the UBF and Ca II K₃ images were obtained by stepping a $0''.6 \times 84''$ slit 250 times across the $130''$ FOV in $0''.525$ steps. At each slit position full Stokes spectra of the photospheric Zeeman-sensitive Fe I $\lambda\lambda 6301.5$ 6302.5 lines were recorded with a slit integration time of ~ 4.5 s, resulting in a complete map integration time of ~ 19 minutes.

3. DATA REDUCTION AND ANALYSIS

3.1. Photospheric Vector Magnetograms

The ASP data were reduced and analyzed using the standard ASP software (Skumanich et al. 1997). To extract information on the physical conditions leading to their formation, the observed Stokes I , Q , U , and V profiles were fitted by a nonlinear least-squares inversion to synthesized profiles, obtained from solutions of the polarized radiative transfer equations for a Milne-Eddington model atmosphere (Skumanich & Lites 1987). Although a number of other atmospheric parameters were also obtained by the software, the inversion output parameter in which we are most interested here is the apparent magnetic flux density

$$B_{\text{app}} = |B|f \cos(\psi), \quad (1)$$

where $|B|$ is the magnetic field strength, f is the fill fraction, and ψ is the inclination angle of the magnetic vector from the line of sight.

A sample map obtained with the ASP is shown in Figure 1d, where the NBPs considered in this study are labeled. Good spatial agreement exists between the labeled areas of magnetic flux and the regions of enhanced emission observed in the filtergram FOVs, shown in Figures 1a–1c. Apparent flux density values were determined for each NBP by averaging over all nonzero pixels (i.e., those reliably fitted by the inversion procedure) in the vicinity of a filtergram brightening. Some NBPs were not detected in the later ASP maps because of degraded seeing conditions. Hence, the flux density value from the first map was compared to those obtained from two maps taken over a period ~ 1 – 2 hr previously. As there was no significant change, it was assumed the flux density had remained approximately constant throughout our observing sequence, and the values from the clearest map taken before the time series were adopted.

TABLE 1
DETAILS OF IMAGE ACQUISITION

Line Observed	Central Wavelength (Å)	Filter Bandpass (Å)	Exposure Time (s)	Height of Formation (km)
Ca II K ₃	3933.68	0.30	1.5	1800–2000 ^a
H α core	6562.81	0.21 ^b	0.3	1200–1700 ^a
Mg I $b_1 - 0.4$ Å	5183.22	0.13 ^b	0.9	200 ^c

^a Vernazza et al. 1981.

^b Beckers et al. 1975.

^c Keller & Koutchmy 1991.

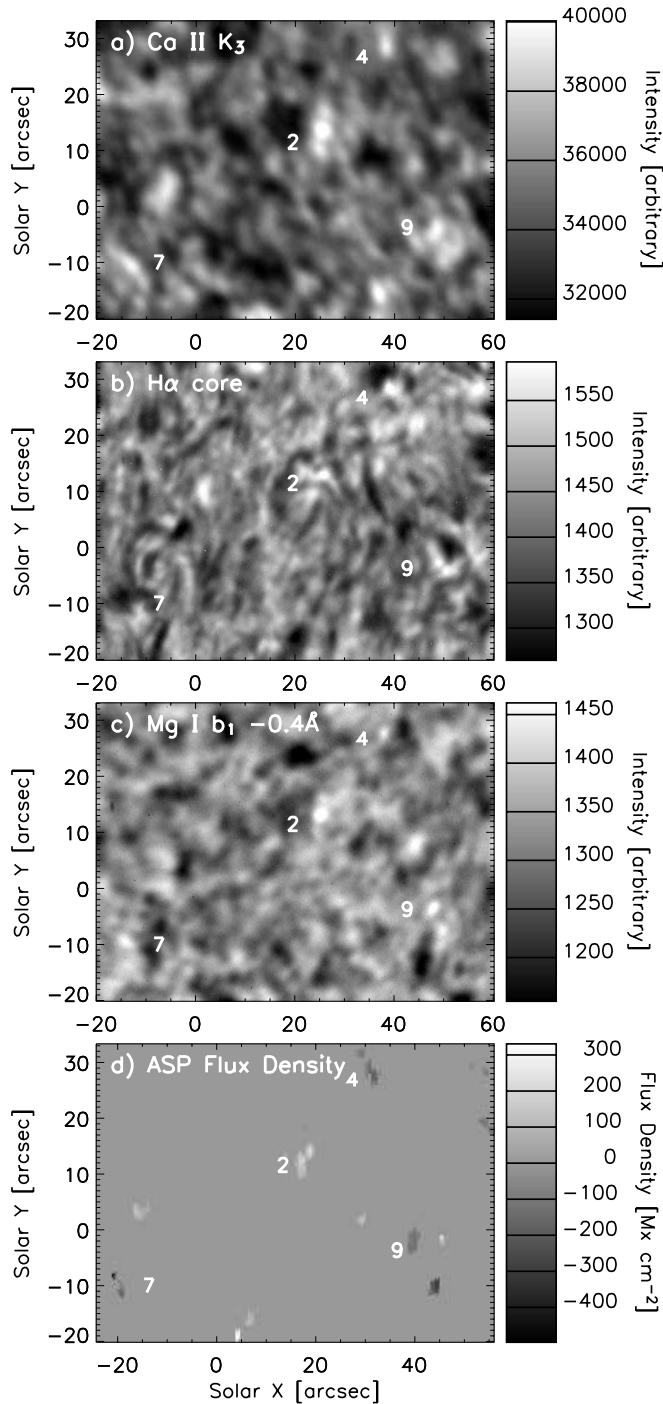


FIG. 1.—Partial FOVs for (a) Ca II K₃, (b) H α , (c) Mg I b₁ - 0.4 Å, and (d) ASP data. Scales shown on the right depict gray scales of intensity in arbitrary units for (a–c), while for plot (d) the apparent magnetic flux density is in units of Mx cm⁻². Numbers overlaid in all panels mark the NBP number assignments.

3.2. Chromospheric Images

The UBF and Ca II K₃ images were reduced and analyzed using standard routines within the SolarSoftWare (Freeland & Handy 1998) tree of IDL. First, all data were flat-fielded and dark-subtracted. At each wavelength, all images were then aligned to the middle image of the series through cross-correlation.

3.2.1. Light Curve Construction

Light curves for each NBP were created using a method similar to that discussed by McAteer et al. (2002, 2003). A brief

summary of this method is provided here. NBPs were determined as those regions of enhanced brightening in the time-averaged Ca II K₃ and Mg I b₁ filtergrams that also have detectable ASP photospheric magnetic flux. Subfields centered on each NBP were then extracted, and individual NBP light curves were obtained. Several previous studies have employed threshold levels that are some multiple of standard deviations σ above the time-averaged background intensity level, using this constant intensity value throughout the image sequence. However, adopting a constant intensity value for the entire time series may lead to (1) erroneous sampling of any brightening within the subfield that occurs above the threshold level; (2) nonselection of an NBP if the subfield dims because of thin clouds; and (3) sampling of different amounts of the NBP in different images, as the distribution of pixel values can vary significantly from one image to another. Others have taken a more statistically correct approach by using the “contour-and-contrast” method. In our analysis, to ensure that pixels contributing to the light curve were caused only by the NBP under consideration, only those pixels within a closed contour around the NBP maximum were selected. The threshold intensity level of each contour is taken to be a fixed multiple of σ above each individual image background intensity level. McAteer et al. (2003) define this level as the maximum multiple of σ above the image background for which each image contour in the time series contains at least 10 pixels. Individual thresholds are determined for each passband so as to sample the same area of the NBP core. Defining the image background as the modal pixel value, I_i^{mod} , and the NBP intensity as the average pixel value within the closed contour, I_i^{ave} , the NBP contrast value, I_i^{con} , for image i in a sequence of images is

$$I_i^{\text{con}} = \frac{I_i^{\text{ave}} - I_i^{\text{mod}}}{I_i^{\text{ave}} + I_i^{\text{mod}}}, \quad (2)$$

and the resulting light curve is a sequence of contrast values. If the NBP moves inside the subfield, care must be taken to follow the same NBP and prevent the contouring of erroneous maxima. For this reason we incorporate a “wander region” within the subfield. Any brightening outside this region is not considered in the selection of the NBP maximum, allowing localized spatial tracking of the NBP.

3.2.2. Wavelet Correlations

We perform both wavelet analysis (Torrence & Compo 1998) and Fourier analysis on all light curves in all wavelengths. In § 4 we utilize Fourier power to study the height variation of detected wave modes. The use of wavelet analysis as well as Fourier analysis stems from the additional information provided on the temporal evolution of oscillatory power, which is especially useful when considering the quasi-periodic nature of these oscillations. The wavelet analysis was carried out using a Morlet wavelet: the product of a sinusoidal wave and a Gaussian envelope. Wavelet power transforms give both spectral and temporal information (Figs. 2a and 2c) but include a cone of influence (COI) at the beginning and end of the time series, where edge effects become important. The extent of the COI at any period P is defined as the wavelet decorrelation time, which for the Morlet wavelet has the form $t_d = \sqrt{2}P/1.03$. To be certain that wavelet power is not erroneous, we require significant power of at least t_d duration outside the COI. However, with increasing period of oscillation the COI becomes larger, leaving less of the time

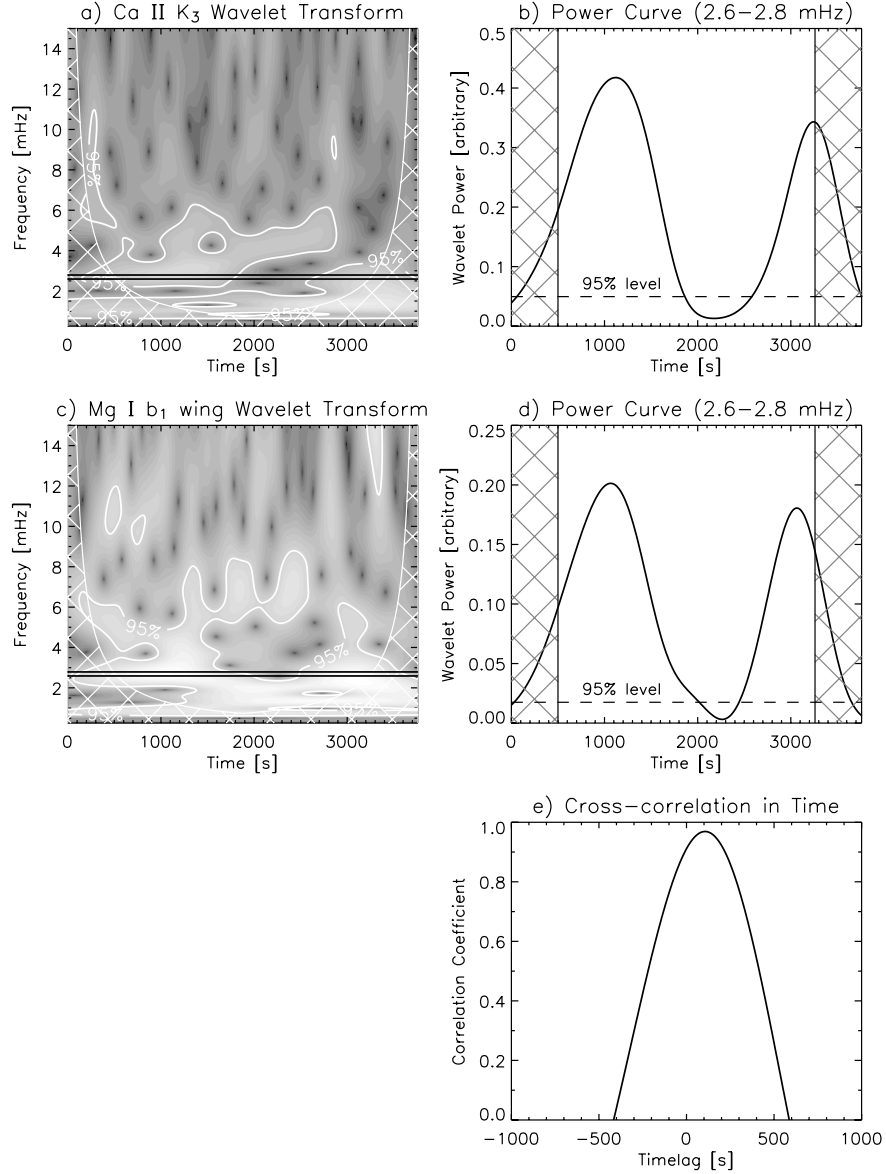


FIG. 2.—Sample wavelet plots for NBP 4. (a) Ca II K₃ wavelet power transform, where lighter shades correspond to increased power. The hatched zone marks out the COI, while the contour follows the 95% confidence level. (b) Power curve constructed by averaging Ca II K₃ wavelet power across frequency in the band 2.6–2.8 mHz, outlined in (a) by two solid horizontal black lines. Again, the hatched areas mark the COI, and the dashed line shows the 95% confidence level. Values of wavelet power are given in arbitrary units, since wavelet power transforms were not normalized. This prevents direct comparison between values of power curves obtained in different wavelengths. (c) Same as (a), but for Mg I b₁ – 0.4 Å. (d) Same as (b), but for Mg I b₁ – 0.4 Å. (e) Correlation curve achieved through cross-correlating the curves shown in (b) and (d) in time.

series available outside the COI. Hence, there is a period at which only t_d remains outside the COI (i.e., the total time series duration, D_{tot} , equates to $3t_d$), given by $P_{\text{max}} = 1.03D_{\text{tot}}/3\sqrt{2}$. For our time series of 3760 s, this means that periods greater than 913 s cannot satisfy the significant wavelet detection criterion. Hence, all light curves were high-pass-filtered with a cutoff of 1.1 mHz. This was achieved through the convolution of the time series with a suitable Bessel function.

Having determined a wavelet power transform for the filtered time series, the correlation (and hence time lag) between wavelet power for two wavelengths, λ_1 and λ_2 , can be determined as a function of frequency ν . In each wavelength, at each frequency, a power curve was obtained by averaging a slice of the wavelet power transform over a frequency band (Figs. 2b and 2d). For comparison with previous work, we utilize overlapping bands of width 0.2 mHz, stepped by

0.005 mHz. For each frequency band, the two power curves, $P_{\lambda_1}(t, \nu)$ and $P_{\lambda_2}(t, \nu)$, were then cross-correlated in time. The cross-correlation coefficient, $C(\Delta t, \nu)$, of these curves as a function of shift in time, Δt , is given by³

$$C(\Delta t, \nu) = \frac{\sum [P_{\lambda_1}(t, \nu) - \overline{P_{\lambda_1}(t, \nu)}][P_{\lambda_2}(t + \Delta t, \nu) - \overline{P_{\lambda_2}(t + \Delta t, \nu)}]}{\sqrt{\sum [P_{\lambda_1}(t, \nu) - \overline{P_{\lambda_1}(t, \nu)}]^2 \sum [P_{\lambda_2}(t, \nu) - \overline{P_{\lambda_2}(t, \nu)}]^2}}, \quad (3)$$

³ We note that this correlation equation was stated incorrectly in our previous paper (eq. [4] in McAteer et al. 2003). We have used equation (3) in the form given here for the analysis in both papers.

allowing the determination of the shift required in $P_{\lambda_1}(t, \nu)$ to give maximum correlation to $P_{\lambda_2}(t, \nu)$ (Fig. 2e). This shift is taken to represent the time required for a wave to travel from the formation height of λ_2 to that of λ_1 . Knowledge of the difference in the formation heights of λ_1 and λ_2 (Table 1) can then be used to calculate the speed of the wave at each frequency (Bocchialini & Baudin 1995; Baudin, Bocchialini, & Koutchmy 1996). Improved cadence over previous studies (10 s, compared to 45 s in McAteer et al. 2003) permits a better determination of the wave speeds, as the correlation in time can be resolved to smaller increments.

A sample correlation diagram for two wavelengths is shown in Figure 3. In this plot, frequency values correspond to the midpoints of the wavelet power slices, and each has a maximum correlation coefficient and time lag associated with it. Candidates for individual waves are identified as peaks in the frequency against maximum correlation coefficient curve (Fig. 3, *top left*). One such example is the good correlation peak of 0.97 close to 2.7 mHz. Each peak is assumed to have a ± 0.1 mHz associated range because of the 0.2 mHz frequency bandwidth employed in the power curve construction. The range of time lags associated with a wave can then be determined by tracing across to the symbols and down to the axis in the time lag against peak correlation coefficient curve (Fig. 3, *top right*). Alternatively, one may trace down to the symbols and across to the axis in the frequency against time lag curve (Fig. 3, *bottom*). Following this, the correlation peak previously mentioned near 2.7 mHz clearly corresponds to the time lag values clustered around 100 s in both time lag curves. By way of completeness, this correlation peak lies within the frequency range over which the power slices in Figures 2b and 2d were obtained. Again, Figure 2e shows the peak correlation coefficient at time lag ~ 100 s.

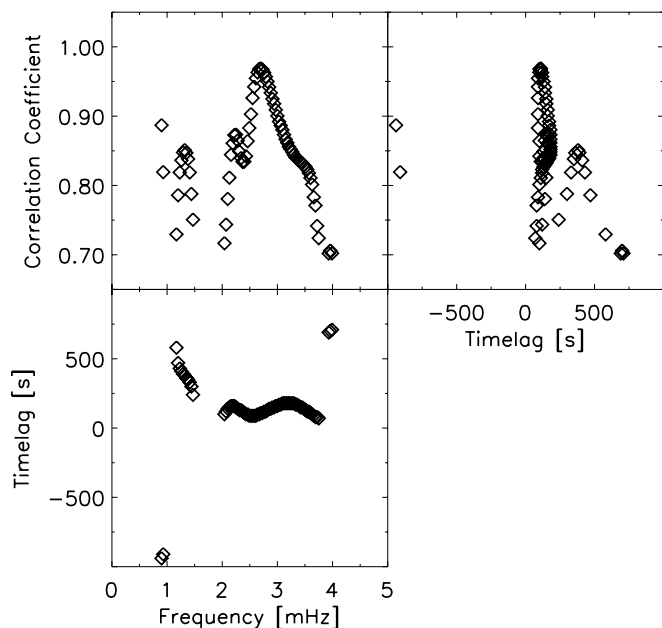


FIG. 3.—Wave correlation diagram constructed from correlation in time between wavelet power slices of $\text{Mg I } b_1 - 0.4 \text{ \AA}$ and Ca II K_3 in NBP 4, where only those data points with correlation coefficients greater than 0.7 are displayed. *Top left*: Frequency against maximum correlation coefficient curve. *Top right*: Time lag against maximum correlation coefficient curve. *Bottom*: Frequency against time lag curve.

3.2.3. Wave Criteria

To determine whether an oscillation corresponds to a possible wave, we apply the following criteria to the Fourier spectra, wavelet power transforms, and wavelet power correlations, respectively:

1. The Fourier power must be above the 95% confidence level.
2. The wavelet power must be above the 95% confidence level for longer than t_d outside the COI.
3. The peak correlation coefficients between wavelet power curves must be above 0.7.

Having arrived at a number of waves, the likelihood of their involvement in mode coupling is determined by applying the following tests (Kalkofen 1997):

1. Both upwardly propagating transverse-mode waves, at frequency ν_κ , and longitudinal-mode waves propagating to the same or greater atmospheric height, at frequency ν_λ ($\approx 2\nu_\kappa$), must be detected within the same NBP.
2. Fourier power at frequency ν_κ in the lower chromosphere should be observable higher in the atmosphere at reduced power.
3. Fourier power at frequency ν_λ should appear in the upper atmosphere.
4. Waves remaining at or above the transverse cutoff frequency ν_κ after coupling should propagate at around the sound speed ($\sim 8 \text{ km s}^{-1}$).

4. RESULTS AND DISCUSSION

4.1. Wavelet and Fourier Analyses

In our study of 11 NBPs we have found a total of 80 traveling waves. Of these, 40 were found to propagate up through the atmosphere, with the remaining 40 traveling down. We find evidence for four cases of mode coupling involving eight upward waves (20% of upward waves or 10% of all waves). These cases were distributed among four of the 11 NBPs studied here, yielding $\sim 1/3$ mode-coupling cases per NBP studied, with no NBP displaying more than one mode-coupling case. Three of the detected mode-coupling, transverse-mode frequencies are in the range 1.2–1.6 mHz, with the remaining case being 2.0–2.2 mHz. Subsequently, three of our cases have longitudinal-mode frequencies over the range 2.6–3.2 mHz, with the final case being 3.9–4.1 mHz. Excellent agreement is reached between our values and those of 1.3 and 1.9 mHz for transverse cases and 2.6 and 3.8 mHz for longitudinal cases previously found by McAteer et al. (2003). By studying the changes in Fourier power and durations of significant wavelet detections, we found that after mode coupling two of our cases show a decrease in longitudinal-mode Fourier power with increasing height, taken here as dissipation of the waves.

Information on those waves satisfying criteria for mode coupling is summarized in Table 2. Details on the range of wave frequencies, the formation regions between which the wave correlation was found, the range of correlation coefficients in time, resulting wave speeds, and attributed MHD wave modes are all displayed. Detections across multiple correlations at similar frequencies have been grouped together and are treated as a single wave. Waves that exhibit a zero time lag have speeds followed by a plus sign. These indicate lower limits to the maximum speed, determined from the

TABLE 2
SUMMARY OF MODE-COUPLING WAVE FREQUENCIES, CORRELATIONS, SPEEDS, AND MODES

NBP	FREQUENCY (mHz)	Correlation Regions		CORRELATION COEFFICIENT	SPEED (km s ⁻¹)	MHD MODE
		λ_2	λ_1			
2.....	1.16–1.36	H α	Ca II K ₃	0.95–0.98	1.1–80+	
	1.17–1.37	Mg I b_1 – 0.4 Å	Ca II K ₃	0.92–0.99	5.2–180+	Tran. ^a
	1.21–1.41	Mg I b_1 – 0.4 Å	H α	0.96–0.99	3.2–150+	Tran. ^b
4.....	2.65–2.85	Mg I b_1 – 0.4 Å	Ca II K ₃	0.97–0.99	53.3–180+	Long. ^{a, b}
	1.23–1.43	Mg I b_1 – 0.4 Å	Ca II K ₃	0.81–0.85	3.6–5.6	Tran. ^c
		Mg I b_1 – 0.4 Å	H α	0.80–0.84	3.2–7.1	Tran. ^d
7.....	2.59–2.79	Mg I b_1 – 0.4 Å	Ca II K ₃	0.95–0.97	13.3–20	Long. ^{c, d}
	2.01–2.21	Mg I b_1 – 0.4 Å	Ca II K ₃	0.96–0.98	26.7–180+	Tran. ^e
	3.91–4.11	Mg I b_1 – 0.4 Å	H α	0.84–0.85	3.2–5.2	Long. ^e
9.....	1.35–1.55	H α	Ca II K ₃	0.68–0.77	1.1–20	Tran. ^f
	2.99–3.19	Mg I b_1 – 0.4 Å	Ca II K ₃	0.88–0.91	2.4–2.8	Long. ^f

^a Transverse-mode wave found at 1.2–1.4 mHz in Mg I b_1 to Ca II K₃, at speeds encompassing the sound speed; longitudinal-mode wave found at 2.7–2.9 mHz in Mg I b_1 to Ca II K₃.

^b Transverse-mode wave at 1.2–1.4 mHz, in Mg I b_1 to H α at speeds encompassing the sound speed; longitudinal-mode wave found at 2.7–2.9 mHz in Mg I b_1 to Ca II K₃.

^c Transverse-mode wave found at 1.2–1.4 mHz in Mg I b_1 to Ca II K₃ at speeds slightly below the sound speed; longitudinal-mode wave found at 2.6–2.8 mHz in Mg I b_1 to Ca II K₃.

^d Transverse-mode wave found at 1.2–1.4 mHz in Mg I b_1 to H α at speeds slightly below the sound speed; longitudinal-mode wave found at 2.6–2.8 mHz in Mg I b_1 to Ca II K₃.

^e Transverse-mode at 2.0–2.2 mHz from Mg I b_1 to Ca II K₃, at speeds above the sound speed; longitudinal-mode wave found at 3.9–4.1 mHz in Mg I b_1 to H α .

^f Transverse-mode found at 1.4–1.6 mHz in H α to Ca II K₃, at speeds encompassing the sound speed; longitudinal-mode wave found at 3.0–3.2 mHz in Mg I b_1 to Ca II K₃.

smallest nonzero time lag achieved. Footnote descriptions for the transverse (labeled “Tran.”) and longitudinal (labeled “Long.”) modes show which waves are believed to be related through mode coupling. Those descriptions with a common letter are involved in the same case of mode coupling, while the numbers indicate multiple detections of a mode-coupling case over different wave correlations. It must be noted that test 1 in § 3.2.3 requires mode-coupling cases to have a longitudinal mode observed over the same correlation height

range, or a range extending higher in the atmosphere than that over which the transverse mode was found.

In conjunction with this summary, Table 3 shows the Fourier power (FP) associated with the transverse and longitudinal modes for each formation height. The values of power displayed are for normalized Fourier spectra (such that noise has an rms value of 1), allowing direct comparisons to be made between Fourier spectra of different time series. This means that confidence levels attributed to these spectra are at

TABLE 3
VARIATION OF NORMALIZED FOURIER POWER AND DURATION OF SIGNIFICANT WAVELET DETECTION WITH ATMOSPHERIC HEIGHT

NBP	FREQUENCY (mHz)	MHD MODE	NORMALIZED FOURIER POWER ^a		
			Mg I b_1 – 0.4 Å	H α CORE	Ca II K ₃
2.....	1.33	Tran. ^b	<i>20.4</i>	42.2	8.2
	2.66	Long. ^c	20.6*	...	48.0*
4.....	1.33	Tran. ^d	30.5	11.2	29.5
	2.66	Long. ^e	50.7*	16.8*	36.1*
7.....	2.12	Tran. ^f	36.5*	7.8*	11.1
	4.24	Long. ^g	7.1	18.0*	13.4
9.....	1.59	Tran. ^h	22.9	31.5*	13.4*
	3.18	Long. ⁱ	...	15.2*	9.5*

NOTE.—For transverse and longitudinal mode-coupling waves.

^a Duration of wavelet detection: ($<1t_d$) shown in italics; ($1t_d-2t_d$) normal text; ($>2t_d$) marked with asterisks.

^b Transverse-mode waves found at 1.2–1.4 mHz in Mg I b_1 to Ca II K₃ and Mg I b_1 to H α , both at speeds encompassing the sound speed (labeled a and b Table 2, respectively).

^c Longitudinal-mode wave found at 2.7–2.9 mHz in Mg I b_1 to Ca II K₃ (labeled a, b in Table 2).

^d Transverse-mode waves found at 1.2–1.4 mHz in Mg I b_1 to Ca II K₃ and Mg I b_1 to H α , both at speeds slightly below the sound speed (labeled c and d in Table 2, respectively).

^e Longitudinal-mode wave found at 2.6–2.8 mHz in Mg I b_1 to Ca II K₃ (labeled c, d in Table 2).

^f Transverse-mode wave found at 2.0–2.2 mHz in Mg I b_1 to Ca II K₃, at speeds above the sound speed (labeled e in Table 2).

^g Longitudinal-mode wave found at 3.9–4.1 mHz in Mg I b_1 to H α (labeled e in Table 2).

^h Transverse-mode wave found at 1.4–1.6 mHz in H α to Ca II K₃, at speeds encompassing the sound speed (labeled f in Table 2).

ⁱ Longitudinal-mode wave found at 3.0–3.2 mHz in Mg I b_1 to Ca II K₃ (labeled f in Table 2).

TABLE 4
MAGNETIC FLUX DENSITY VALUES FOR NBPs DISPLAYING
MODE COUPLING

NBP	Mean Apparent Magnetic Flux Density (Mx cm ⁻²)
2.....	108
4.....	-111
7.....	-142
9.....	-99

their χ^2 percentage value, placing the 95% level at a value of 5.99 and the 99% level at 9.21 for this table. A further depiction of the quality of evidence for the wave modes at each height is the duration of significant wavelet detection, relating to the second point in the first list in § 3.2.3. This is depicted here in terms of ranges of significant wavelet detection: no detection ($<1t_d$, italic), a marginal duration of 1–2 decorrelation lifetimes ($1t_d$ – $2t_d$) in normal text, or a more robust detection of more than 2 decorrelation lifetimes ($>2t_d$, marked with asterisks). In line with the wave criteria given in § 3.2.3, if no significant FP is present, then no indication of the duration of wavelet detection is shown, irrespective of its existence. For completeness, the mean photospheric apparent magnetic flux density of each NBP involved in mode coupling is also displayed in Table 4.

4.1.1. NBP 2

As can be seen from inspection of Table 2, there exists a possible transverse-mode wave at 1.2–1.4 mHz, observed in $H\alpha$ to Ca II K₃, Mg I b₁ to Ca II K₃ (marked by footnote a), and Mg I b₁ to $H\alpha$ (footnote b) at speeds encompassing the sound speed (test 4). The corresponding longitudinal-mode wave for Mg I b₁ to Ca II K₃ is seen at 2.7–2.9 mHz (test 1). The variation of FP with atmospheric height is depicted in Table 3 for the closest possible Fourier frequencies, 1.33 and 2.66 mHz. This shows comparable FP in both the transverse and longitudinal modes at the height of Mg I b₁, although only the longitudinal mode displays a significant wavelet duration. An increase in the transverse-mode FP, with an onset of fairly significant wavelet duration, and a lack of longitudinal-mode FP is seen in the $H\alpha$ level. At the height of Ca II K₃ formation, the transverse-mode FP decreases (test 2) and significant wavelet duration disappears, while large longitudinal-mode FP appears (test 3), accompanied by significant wavelet duration. This suggests that the transfer of power involved in mode coupling occurs between the regions of $H\alpha$ and Ca II K₃ formation. The apparent flux density value obtained for this NBP was 108 Mx cm⁻².

4.1.2. NBP 4

Similar to the previous NBP, this exhibits one possible case of mode coupling. In Table 2 the transverse-mode wave is found at 1.2–1.4 mHz in both Mg I b₁ to Ca II K₃ (footnote c) and Mg I b₁ to $H\alpha$ (footnote d) at speeds slightly below the sound speed (test 4). The corresponding longitudinal-mode wave is seen at 2.6–2.8 mHz for only the Mg I b₁ to Ca II K₃ correlation (test 1). The Fourier frequencies associated with this possible mode-coupling case, 1.33 and 2.66 mHz, are again displayed in Table 3. At Mg I b₁ both the transverse and longitudinal modes display high levels of FP, where the longitudinal mode shows a greater level of power and duration of wavelet. The $H\alpha$ level shows both

modes decreasing quite drastically in FP (test 2), with the longitudinal mode maintaining wavelet significance while the transverse mode loses its significant wavelet altogether. Strangely, by Ca II K₃ both modes exhibit an increase in the level of their FP, remaining below the level of Mg I b₁ FP, with no changes in their wavelet significances. This odd $H\alpha$ behavior may be due to the complexity and confusion in assigning NBPs at this wavelength. These variations in FP with formation height lead us to believe that power transfer had already taken place before or at the height of Mg I b₁. An apparent flux density of -111 Mx cm⁻² was detected for this NBP.

4.1.3. NBP 7

Table 2 shows a transverse mode at 2.0–2.2 mHz from Mg I b₁ to Ca II K₃ (footnote e), at speeds above the sound speed. The resulting longitudinal mode is seen at 3.9–4.1 mHz (test 1). Variations in the power of the Fourier frequencies 2.12 and 4.24 mHz are depicted in Table 3. The formation height of Mg I b₁ has large transverse-mode FP with long duration of significant wavelets, while the longitudinal mode has low FP with fairly significant wavelet duration at this height. $H\alpha$ shows a marked decrease in transverse-mode FP (test 2), although retaining long significant wavelet duration, with an increase in FP by a factor of more than 2 for the longitudinal mode (test 3) and longer significant wavelet duration. At Ca II K₃ the transverse mode exhibits a marginal increase in FP and loss of wavelet significance, while the longitudinal mode decreases in both FP and significant wavelet duration. This would suggest that the height at which mode-coupling power transfer occurs is between Mg I b₁ and $H\alpha$. The apparent flux density for this NBP was observed to be -142 Mx cm⁻².

4.1.4. NBP 9

The transverse mode for $H\alpha$ to Ca II K₃ (footnote f) was found at 1.4–1.6 mHz, having speeds encompassing the sound speed (test 4). The longitudinal-mode detection associated with this was observed at 3.0–3.2 mHz (test 1). Table 3 shows the development of FP with height for the Fourier frequencies 1.59 and 3.18 mHz. Only transverse-mode FP is seen at Mg I b₁ with a fairly good significant wavelet duration. This transverse-mode FP is observed to increase in both Fourier and wavelet significance in $H\alpha$, while longitudinal-mode FP begins at long significant wavelet duration (test 3). By Ca II K₃ both modes have decreased in their levels of FP (test 2) while retaining their long durations of significant wavelets. The variation of FP observed leads to the belief that transfer of power occurs between the heights of Mg I b₁ and $H\alpha$. This NBP displayed an apparent flux density of -99 Mx cm⁻².

5. CONCLUSIONS

We have presented four detections of MHD mode coupling occurring in the quiet-Sun network. The corresponding variations in Fourier power with height show two cases exhibiting dissipation of their longitudinal modes. This adds plausibility to the concept of chromospheric heating arising in part from the transport of photospheric energy into the chromosphere by nondamping transverse MHD modes. The subsequent transfer of energy to longitudinal modes enables the deposition of this energy into the surrounding plasma by the shocking of these waves in the mid- to high chromosphere. Transverse-mode frequencies seen in three of the detected

mode-coupling cases occur over the range 1.2–1.6 mHz, with the remaining case showing 2.0–2.2 mHz, while again three of our cases have longitudinal-mode frequencies grouped in the 2.6–3.2 mHz range, with the final case being 3.9–4.1 mHz. These values are in excellent agreement with those previously found by McAteer et al. (2003), who found transverse modes at 1.3 and 1.9 mHz and longitudinal modes at 2.6 and 3.8 mHz. Interestingly, the three cases that show tighter grouping of mode-coupling frequencies (those with transverse modes over 1.2–1.6 mHz) have mean apparent flux density magnitudes in the range 99–111 Mx cm^{-2} , while the final case (transverse mode over 2.0–2.2 mHz) has a greater value of 142 Mx cm^{-2} .

Further studies should include higher cadence vector magnetograms, enabling a temporal study of the evolution in NBP flux densities. Additional, more pronounced oscillatory information from Doppler velocities could prove useful if spectral maps can be obtained at sufficiently high cadence. Obtaining spectral maps rather than filtergram images would also yield better coverage of atmospheric height through the ability to sample intensity at varying distances into the line wings. Such an approach could enable the study of mode-coupling height as a function of NBP flux density.

This work was supported by the UK Particle Physics and Astronomy Research Council. Both D. S. B. and J. M. A. are supported by Northern Ireland Department for Employment and Learning studentships. J. M. A. also thanks Queen's University Belfast for a CAST studentship. F. P. K. is grateful to A. W. E. Aldermaston for the award of a William Penney Fellowship. Observations were obtained at the National Solar Observatory, operated by the Association of Universities for Research in Astronomy, Inc. (AURA), under cooperative agreement with the National Science Foundation. Additional invaluable help on using the ASP reduction and analysis software was provided by B. Lites at the High Altitude Observatory. We also thank S. Hasan for useful discussion and the referee, R. Rutten, for constructive comments on the manuscript. Finally, we would like to thank the observers at the DST for perseverance in the face of abominable weather conditions and an adverse Miller moth population. Wavelet software was provided by C. Torrence and G. P. Compo.⁴

⁴ Wavelet software is available at <http://paos.colorado.edu/research/wavelets>.

REFERENCES

- Baudin, F., Bocchialini, K., & Koutchmy, S. 1996, *A&A*, 314, L9
 Beckers, J. M., Dickson, L., & Joyce, R. S. 1975, A Fully Tunable Lyot-Öhman Filter (AFCRL-TR-75-0090; Bedford: AFCRL)
 Berger, T. E., & Title, A. M. 2001, *ApJ*, 553, 449
 Bocchialini, K., & Baudin, F. 1995, *A&A*, 299, 893
 Carlsson, M., & Stein, R. F. 1997, *ApJ*, 481, 500
 Cauzzi, G., Falchi, A., & Falciani, R. 2000, *A&A*, 357, 1093
 Damé, L., Gouttebroze, P., & Malherbe, J.-M. 1984, *A&A*, 130, 331
 Elmore, D. F., et al. 1992, *Proc. SPIE*, 1746, 22
 Freeland, S. L., & Handy, B. N. 1998, *Sol. Phys.*, 182, 497
 Goodman, M. L. 2000, *ApJ*, 533, 501
 Hasan, S. S., & Kalkofen, W. 1999, *ApJ*, 519, 899
 Hasan, S. S., Kalkofen, W., van Ballegooijen, A. A., & Ulmschneider, P. 2003, *ApJ*, 585, 1138
 Kalkofen, W. 1997, *ApJ*, 486, L145
 Keller, C. U., & Koutchmy, S. 1991, *ApJ*, 379, 751
 Kneer, F., & von Uexküll, M. 1985, *A&A*, 144, 443
 ———. 1986, *A&A*, 155, 178
 Lites, B. W., Rutten, R. J., & Kalkofen, W. 1993, *ApJ*, 414, 345
 McAteer, R. T. J., Gallagher, P. T., Williams, D. R., Mathioudakis, M., Bloomfield, D. S., Phillips, K. J. H., & Keenan, F. P. 2003, *ApJ*, 587, 806
 McAteer, R. T. J., Gallagher, P. T., Williams, D. R., Mathioudakis, M., Phillips, K. J. H., & Keenan, F. P. 2002, *ApJ*, 567, L165
 Musielak, Z. E., & Ulmschneider, P. 2003a, *A&A*, 400, 1057
 ———. 2003b, *A&A*, 406, 725
 Rutten, R. J., & Uitenbroek, H. 1991, *Sol. Phys.*, 134, 15
 Schrijver, C. J., Title, A. M., van Ballegooijen, A. A., Hagenaar, H. J., & Shine, R. A. 1997, *ApJ*, 487, 424
 Skumanich, A., & Lites, B. 1987, *ApJ*, 322, 473
 Skumanich, A., Lites, B., Martinez Pillet, V., & Seagraves, P. 1997, *ApJS*, 110, 357
 Torrence, C., & Compo, G. P. 1998, *Bull. Am. Meteorol. Soc.*, 79, 61
 Vernazza, J. E., Avrett, E. H., & Loeser, R. 1981, *ApJS*, 45, 635
 von Uexküll, M., Kneer, F., Malherbe, J. M., & Mein, P. 1989, *A&A*, 208, 290
 Zhugzhda, Y. D., Bromm, V., & Ulmschneider, P. 1995, *A&A*, 300, 302

ERRATUM: “PROPAGATING WAVES AND MAGNETOHYDRODYNAMIC MODE COUPLING
IN THE QUIET-SUN NETWORK” (ApJ, 604, 936 [2004])

D. SHAUN BLOOMFIELD, R. T. JAMES McATEER, MIHALIS MATHIOUDAKIS,
DAVID R. WILLIAMS, AND FRANCIS P. KEENAN

Proof corrections were not carried correctly to the final printed version of this paper, which resulted in an extra set of overbars appearing in both terms of the denominator of equation (3). The correct form of this equation is:

$$C(\Delta t, \nu) = \frac{\sum [P_{\lambda_1}(t, \nu) - \overline{P_{\lambda_1}(t, \nu)}] [P_{\lambda_2}(t + \Delta t, \nu) - \overline{P_{\lambda_2}(t + \Delta t, \nu)}]}{\sqrt{\sum [P_{\lambda_1}(t, \nu) - \overline{P_{\lambda_1}(t, \nu)}]^2 \sum [P_{\lambda_2}(t, \nu) - \overline{P_{\lambda_2}(t, \nu)}]^2}}. \quad (3)$$

As noted in footnote 3, this correlation equation was stated incorrectly in our previous paper (eq. [4] in R. T. J. McAteer et al., ApJ, 587, 806 [2003]). However, the correct form of equation (3), now given here, was used for the analysis in both papers.

The press sincerely regrets this error.